Investigation of a bistable dual-stage vibration isolator under harmonic excitation

2014 Smart Mater. Struct. 23 045033

(http://iopscience.iop.org/0964-1726/23/4/045033)

IOP Publishing Smart Materials and Structures
Smart Mater. Struct. **23** (2014) 045033 (11pp) doi:10.1088/0964-1726/23/4/045033

Investigation of a bistable dual-stage vibration isolator under harmonic excitation

Kai Yang[1,2], R L Harne[2], K W Wang[2] and Hai Huang[1]

[1] School of Astronautics, Beihang University, Beijing 100191, People's Republic of China
[2] Department of Mechanical Engineering, University of Michigan, Ann Arbor, MI 48109-2125, USA

E-mail: yangkai@sa.buaa.edu.cn

Received 30 October 2013, revised 17 December 2013
Accepted for publication 23 January 2014
Published 10 March 2014

Abstract

This study explores the steady-state performance of a dual-stage vibration isolator, which is configured by a bistable oscillator and a linear oscillator. The potential force of the bistable stage comprises negative linear and positive cubic nonlinear stiffnesses such that the two restoring force contributions may counterbalance to minimize dynamic force transmission. By applying a first-order harmonic balance, it is predicted that the bistable dual-stage isolator may significantly outperform an equivalent pure linear dual-stage isolator. This conclusion is verified through a series of numerical investigations. Following a parametric study, design guidelines are detailed to achieve performance improvements. Then, the 'valley' response, which is the special phenomenon of the bistable dual-stage isolator due to the counterbalance of the negative linear and positive nonlinear potential forces, is revealed and quantitatively explained. Numerical studies demonstrate the role of initial conditions, and it is shown that the likelihood of beneficial single periodic valley and intra-well responses for isolation purposes can be increased by greater bistable stage damping. Finally, a bistable dual-stage isolator prototype is developed and tested, and the numerical and experimental results verify the theoretical predictions.

Keywords: bistable, negative stiffness, nonlinear vibration isolator, dual-stage isolator

(Some figures may appear in colour only in the online journal)

1. Introduction

Vibration degrades the performance of precision instruments and harms the health of structures. A common vibration reduction method is to apply passive isolators. Linear isolator designs are prevalent [1, 2], although they may exhibit the drawback that the low natural frequency required for effective isolation performance conflicts with their capacity to support static load [3]. This deficiency may be overcome by using nonlinear isolators. Ibrahim [4] reviewed various nonlinear isolators and showed that certain design factors and configurations may provide for improved performance over linear counterparts. The nonlinear mechanism, having a negative linear stiffness (NLS), is widely applied to achieve high static yet low dynamic stiffness for wider vibration isolation bandwidth and greater static load supporting capability [3, 5–10]. Many realizations of NLS mechanisms yield both negative linear and positive nonlinear stiffnesses, examples of which are reviewed in the following. Platus [5] proposed an NLS nonlinear mechanism, realized by two horizontal pre-stressed rigid bars. The author combined this mechanism with a linear spring to achieve a low dynamic stiffness isolator to enlarge the effective isolation bandwidth. In the absence of the parallel linear spring connection, the NLS nonlinear mechanism would otherwise induce bistability. With the linear spring, extremely low dynamic stiffness may be realized for vibration isolation purposes. The power flow behaviors and the limitation of lowest fundamental frequency of such isolators were investigated by Yang *et al* [6] and Ahn [7], respectively. Carrella *et al* [3, 8, 9] proposed another NLS nonlinear mechanism configuration using two oblique springs, and found that an isolator combining the mechanism with a linear spring achieves larger isolation bandwidth and greater static load supporting capacity compared to linear

isolators. Then Lu *et al* [10] combined this NLS nonlinear mechanism with a linear spring to configure the upper stage of a dual-stage isolator, and showed that the dual-stage isolator is more effective than a single-stage isolator for isolation at higher frequencies.

In the previous studies, the NLS nonlinear mechanisms were utilized in parallel with linear springs so that zero or small positive linear stiffnesses were ultimately obtained. These configurations provide for the low dynamic and high static stiffnesses of interest while avoiding designs that exhibit bistability. Yet, intuitively, the NLS nonlinear mechanism on its own may be excited in such a way that its potential forces from the negative linear and positive nonlinear stiffnesses could be counterbalanced to minimize dynamic force transmission and improve vibration isolation performance. It is noted that this phenomenon is referred to in other literature as excitation induced stability (EIS) or dynamic stabilization [11–13]. No investigations of NLS mechanism configurations that deliberately exploit EIS for vibration isolation have yet been reported, although experimentally validated design guidelines for obtaining EIS were recently developed [14] and are applicable to this research. However, instead of evaluating NLS mechanism utilization for single-stage vibration isolation, which is comparable to the prior investigations of EIS, this study is motivated by the observations of Lu *et al* [10] in assessing dual-stage nonlinear isolator capabilities. It was demonstrated that a dual-stage isolator with nonlinear and linear stages having positive stiffnesses can realize more rapid roll-off rates at high frequencies than a single-stage isolator, which significantly improves isolation performance [10].

Bringing together the opportunities of EIS for vibration isolation and the advantages of dual-stage isolator design, this paper investigates the steady-state performance of a new dual-stage isolator which consists of an NLS nonlinear first stage and a linear second stage. In contrast to the previous studies, the nonlinear stage retains bistable characteristics which enable it to exploit the feature of force counterbalance for vibration isolation improvement. Utilized in this manner, the bistable first stage has a double-well restoring force potential and may exhibit two different fundamental oscillations: inter-well response where the oscillator symmetrically vibrates around its unstable equilibrium (i.e. snap-through oscillation), and intra-well response (i.e. oscillation around either equilibrium), respectively. This feature has been recently exploited to advance system performance for various applications, including energy harvesting [15, 16], vibration control and damping [17–19], and sensing [20, 21]. Because bistable oscillators are strongly nonlinear and may undergo large oscillations from equilibrium, an appropriate nonlinear analytical method should be selected to predict the response of the present system. The interest in determining the periodic behaviors of the bistable dual-stage isolator encourages use of the harmonic balance method, which is frequently employed to analytically investigate the steady-state response of bistable systems, obtaining qualitatively and quantitatively accurate predictions [22–25]. Based on the analyses, this paper presents insights and guidelines for bistable dual-stage isolator design to yield effective vibration isolation. A quantitative interpretation of the advantageous counterbalance feature of the bistable NLS nonlinear mechanism for vibration isolation is provided. Numerical investigations are performed to uncover initial condition dependences and to shed light on the likelihood of obtaining the beneficial single periodic responses for vibration isolation. Finally, a bistable dual-stage isolator prototype is developed and its responses are numerically and experimentally explored to validate analytical insights.

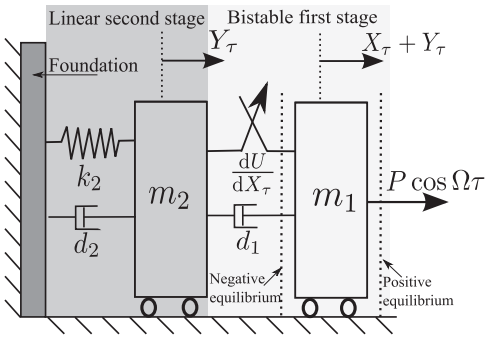

Figure 1. Schematic of the bistable dual-stage isolator.

2. Theory

2.1. Governing equations

Figure 1 depicts the modeled geometry of a bistable dual-stage isolator. This isolator comprises a bistable first stage and a linear second stage. The bistable stage consists of a mass m_1, a damper d_1, and an NLS nonlinear mechanism which has a restoring force potential expressed by $U(X_\tau) = -(1/2)k_1X_\tau^2 + (1/4)k_3X_\tau^4$, where X_τ is the stroke motion of the bistable stage. Thus from the perspective of the schematic in figure 1, it has two stable equilibria, $X_\tau = \pm\sqrt{k_1/k_3}$. The two stable equilibria are symmetric about unstable equilibrium $X_\tau = 0$. This restoring potential form relates to numerous physical realizations of the NLS nonlinear mechanism including axial pre-load and magnetic interactions [15]. The mass, stiffness and damping of the linear second stage are m_2, k_2 and d_2, respectively. The stroke motion of the linear stage is Y_τ. The bistable stage mass m_1 is subjected to a harmonic excitation force denoted by $P\cos\Omega\tau$, in which P, Ω and τ represent the amplitude, frequency and time, respectively. The governing equations are therefore

$$m_1(\ddot{X}_\tau + \ddot{Y}_\tau) + d_1\dot{X}_\tau - k_1X_\tau + k_3X_\tau^3 = P\cos\Omega\tau \quad (1)$$

$$m_2\ddot{Y}_\tau + d_2\dot{Y}_\tau + k_2Y_\tau - d_1\dot{X}_\tau + k_1X_\tau - k_3X_\tau^3 = 0. \quad (2)$$

The transmitted force imposed on the foundation is P_t,

$$P_t = -(k_2Y_\tau + d_2\dot{Y}_\tau). \quad (3)$$

Normalized parameters are defined as

$$\omega_1 = \sqrt{k_1/m_1}; \quad \omega_2 = \sqrt{k_2/m_2}; \quad f = \omega_1/\omega_2;$$
$$\gamma_1 = d_1/m_1\omega_1; \quad \gamma_2 = d_2/m_2\omega_2; \quad \mu = m_1/m_2;$$
$$x = X_\tau\sqrt{k_3/k_1}; \quad y = Y_\tau\sqrt{k_3/k_1};$$
$$p_0 = P\sqrt{k_3}/k_2\sqrt{k_1}; \quad p_t = P_t\sqrt{k_3}/k_2\sqrt{k_1};$$
$$\omega = \Omega/\omega_2; \quad t = \omega_2\tau.$$

Substitution of normalized parameters into equations (1)–(3) leads to a new equation system defined with respect to the normalized time t,

$$x'' + (1+\mu) f\gamma_1 x' - (1+\mu) f^2 x + (1+\mu) f^2 x^3 - \gamma_2 y' - y - (p_0/\mu)\cos\omega t = 0 \quad (4)$$

$$y'' + \gamma_2 y' + y - \mu f\gamma_1 x' + \mu f^2 x - \mu f^2 x^3 = 0 \quad (5)$$

$$p_t = -(y + \gamma_2 y') \quad (6)$$

where operator $(\,)'$ denotes a derivative with respect to t.

2.2. Analytical solution

The first-order harmonic balance method is employed to capture the fundamental dynamics of equations (4)–(6). Since the bistable stage has two dynamic responses, inter- and intra-well, the stroke motions x and y can be expanded as

$$x = c_1(t) + a_1(t)\sin\omega t + b_1(t)\cos\omega t \quad (7)$$

$$y = a_2(t)\sin\omega t + b_2(t)\cos\omega t \quad (8)$$

where $c_1(t) = 0$ and $c_1(t) \neq 0$ represent the inter- and intra-well responses.

Substitution of equations (7)–(8) into equations (4)–(5), assuming slowly varying coefficients, and neglecting higher order terms, leads to five modulation equations with respect to response coefficients,

$$-\gamma_1 c_1' = f\Lambda_c c_1 \quad (9)$$

$$-(1+\mu) f\gamma_1 a_1' + 2\omega b_1' + \gamma_2 a_2' = \Sigma a_1 - \sigma b_1 - a_2 + \omega\gamma_2 b_2 \quad (10)$$

$$-2\omega a_1' - (1+\mu) f\gamma_1 b_1' + \gamma_2 b_2' = \sigma a_1 + \Sigma b_1 - \omega\gamma_2 a_2 - b_2 - p_0/\mu \quad (11)$$

$$\mu f\gamma_1 a_1' - \gamma_2 a_2' + 2\omega b_2' = -\mu f^2\Lambda a_1 + \mu f\omega\gamma_1 b_1 + (1-\omega^2) a_2 - \omega\gamma_2 b_2 \quad (12)$$

$$\mu f\gamma_1 b_1' - 2\omega a_2' - \gamma_2 b_2' = -\mu f\omega\gamma_1 a_1 - \mu f^2\Lambda b_1 + \omega\gamma_2 a_2 + (1-\omega^2) b_2, \quad (13)$$

where the terms are defined as

$$\Lambda_c = -1 + c_1^2 + \frac{3}{2} r_1^2; \qquad \Lambda = -1 + 3c_1^2 + \frac{3}{4} r_1^2;$$

$$\Sigma = (1+\mu) f^2\Lambda - \omega^2; \qquad \sigma = (1+\mu) f\omega\gamma_1;$$

$$r_1 = \sqrt{a_1^2 + b_1^2}; \qquad r_2 = \sqrt{a_2^2 + b_2^2}.$$

Here r_1 and r_2 represent the oscillation amplitudes of motion x and y, respectively.

The steady-state response of the system is now determined. After reduction of equations (10)–(13), a polynomial is obtained, the roots of which represent predicted responses of the bistable stage amplitude squared, r_1^2. The polynomial is found to be

$$r_1^2(\alpha_1\Lambda^2 + \alpha_2\Lambda + \alpha_3) = (p_0/\mu)^2[(1-\omega^2)^2 + (\omega\gamma_2)^2] \quad (14)$$

where

$$\alpha_1 = [f^2 - (1+\mu) f^2\omega^2]^2 + (f^2\omega\gamma_2)^2 \quad (15)$$

$$\alpha_2 = -2f^2\omega^2\{(1-\omega^2)[1-(1+\mu)\omega^2] + (\omega\gamma_2)^2\} \quad (16)$$

$$\alpha_3 = \omega^2\{(1-\omega^2)^2\omega^2 + (f\gamma_1)^2[1-(1+\mu)\omega^2]^2 + \omega^2[(f\gamma_1\gamma_2)^2 + (\omega\gamma_2)^2 + 2\mu f\gamma_1\gamma_2\omega^2]\}. \quad (17)$$

Note that Λ in equation (14) contains unknown c_1, which is determined by steady-state response of equation (9), where $c_1 = 0$ or $c_1^2 = 1 - (3/2)r_1^2$. Hence the amplitude r_1 of either inter- (i.e. $c_1 = 0$) or intra-well (i.e. $c_1^2 = 1 - (3/2)r_1^2$) response is derived. According to equation (6), the force transmissibility is

$$|\mathrm{TR}| = \left|\frac{P_t}{P}\right| = \left|\frac{p_t}{p_0}\right| = \sqrt{1 + (\omega\gamma_2)^2}\left|\frac{r_2}{p_0}\right|. \quad (18)$$

2.3. Stability criterion

It is necessary to identify the stable and unstable solutions of the polynomial (14). Equations (9)–(13) may be rewritten in the form

$$\mathbf{z}' = \mathbf{G}^{-1}\mathbf{F}(\mathbf{z}) \quad (19)$$

where

$$\mathbf{z} = \begin{bmatrix} c_1 \\ a_1 \\ b_1 \\ a_2 \\ b_2 \end{bmatrix},$$

$$\mathbf{G} = \begin{bmatrix} -\gamma_1 & 0 & 0 & 0 & 0 \\ 0 & -(1+\mu) f\gamma_1 & 2\omega & \gamma_2 & 0 \\ 0 & -2\omega & -(1+\mu) f\gamma_1 & 0 & \gamma_2 \\ 0 & \mu f\gamma_1 & 0 & -\gamma_2 & 2\omega \\ 0 & 0 & \mu f\gamma_1 & -2\omega & -\gamma_2 \end{bmatrix}$$

and $\mathbf{F}(\mathbf{z})$ is the right-hand side of equations (9)–(13). The Jacobian matrix of equation (19) is determined from

$$\mathbf{J} = \mathbf{G}^{-1}\left.\frac{\partial \mathbf{F}}{\partial \mathbf{z}}\right|_{\mathbf{z}=\mathbf{z}_s} \quad (20)$$

where $\mathbf{z}_s$ denotes the vector of steady-state solutions. The stable response solutions are ascertained if all eigenvalues of the matrix $\mathbf{J}$ have negative real parts.

3. Isolation performance comparison and 'valley' response

3.1. Comparison with an equivalent linear dual-stage isolator

When the first stage of the isolator is replaced by a linear oscillator, the entire system becomes a linear dual-stage isolator. To provide a meaningful comparison between the isolator designs, it is intuitive that the isolators must provide an identical static loading capacity. Equations (21) and (22) respectively represent the static loadings of the bistable and linear dual-stage isolators.

$$-k_1 X + k_3 X^3 = P \quad (21)$$

$$k_L X = P \quad (22)$$

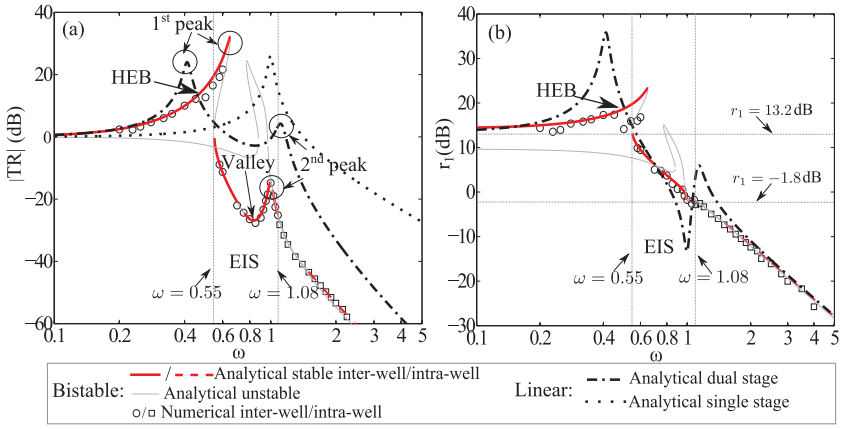

Figure 2. Force transmissibility comparison of bistable dual-stage isolator with an equivalent linear dual-stage isolator and a linear single-stage isolator: (a) force transmissibility; (b) stroke motion amplitudes of the first stage.

where: P is the static load; k_L is the stiffness of the equivalent linear first stage, and thus the natural frequency of this stage is $\omega_L = \sqrt{k_L/m_1}$; X is the deformation subjected to the static load. Using the same approach that normalizes equations (1)–(3), and defining $f_L = \omega_L/\omega_2$ as the frequency tuning ratio of the equivalent linear dual-stage isolator, where ω_2 is the natural frequency of the linear second stage, the parametric relationship between the isolators is

$$f_L^6 + f^2 f_L^4 - f^2(p_0/\mu)^2 = 0. \tag{23}$$

Figure 2(a) plots the force transmissibility of the bistable dual-stage isolator, the equivalent linear dual-stage isolator and a linear single-stage isolator having the same system parameters as the second stage of the linear dual-stage isolator. Figure 2(b) presents the stroke motion amplitudes of the first stages of the dual-stage isolators. The parameters used to predict the responses are as follows: the mass ratio of the first stage mass to the second stage mass is $\mu = 1.0$; the frequency tuning ratio of the first stage to the second stage of the bistable dual-stage isolator is $f = 0.1$; the normalized excitation force amplitude is $p_0 = 1.0$; based on equation (23), the frequency tuning ratio of the equivalent linear dual-stage isolator is $f_L = 0.46$; the loss factors of the first and second stages are $\gamma_1 = 0.10$ and $\gamma_2 = 0.05$, respectively. To validate the analytical predictions of the bistable dual-stage isolator, figure 2 also presents the single periodic responses determined through numerical integration of governing equations (4)–(6) using a fourth-order Runge–Kutta algorithm.

As shown in figure 2, when $\omega \leq 1.08$, the bistable first stage exhibits *inter-well response* (i.e. snap-through oscillation), where its mass oscillates symmetrically around the unstable equilibrium $x = 0$. For the bistable dual-stage isolator, there are two inter-well response branches, the *high-energy branch (HEB)* where the first stage has a large oscillation amplitude, and *excitation induced stability (EIS)*, occurring across the bandwidth $0.55 \leq \omega \leq 1.08$ in this example, where the oscillation amplitude is much smaller (the amplitudes are between $r_1 = -1.8$ dB and $r_1 = 13.2$ dB in figure 2(b)). When $\omega > 1.08$, the bistable stage vibrates around either equilibrium (i.e. *intra-well response*) for the present set of system parameters. In figure 2(a), for the bistable dual-stage isolator, between the frequencies of the two *peaks* ($0.55 \leq \omega \leq 1$), there exists a *valley response* in the EIS frequency band where the vibration is effectively isolated and the maximum attenuation can be nearly 30 dB. In contrast, the linear dual-stage isolator provides much less isolation in the bandwidth between its respective peaks, as figure 2(a). This valley response indicates that the dynamic stiffness of the bistable dual-stage isolator is significantly less than that for the linear dual-stage isolator, and its detailed interpretation will be presented in section 3.2. After the second peak, both dual-stage isolators outperform the single-stage isolator in the high frequency band, because the response slope rates with respect to ω of the bistable and linear dual-stage isolators are twice that of the single-stage isolator as shown in figure 2(a). A clear difference between the amplitudes of the dual-stage isolators' transmissibilities at high frequencies indicates that the bistable dual-stage isolator provides more effective isolation performance when the static loading capacity of the dual-stage systems is identical. Moreover, compared with the linear dual-stage isolator, figure 2(b) shows that the bistable dual-stage isolator can achieve much smaller stroke motion, which reflects the smaller deflection of the bistable oscillator's nonlinear spring. Hence, the bistable dual-stage isolator is more suitable for applications having compact space constraints. These factors encourage further investigation of the source of these advantages for the bistable dual-stage isolator.

For the numerical data points in figure 2 presented as circles and squares for inter-well and intra-well response respectively, the amplitude at each frequency is the fundamental component of single periodic response computed by taking the fast-Fourier transform of the last 35% of the long-time response. Across frequencies, the numerical results are in good agreement with the analytical predictions, validating the model composition and assumptions. Around the valley response in $0.6 \leq \omega \leq 1.0$ and the intra-well response in $1.1 \leq \omega \leq 1.6$, numerical simulations uncovered potential multi-harmonic responses in addition to the single periodic valley (denoted as circles) and intra-well (denoted as rectangles) responses. These behaviors are observed, by repeated simulations of the

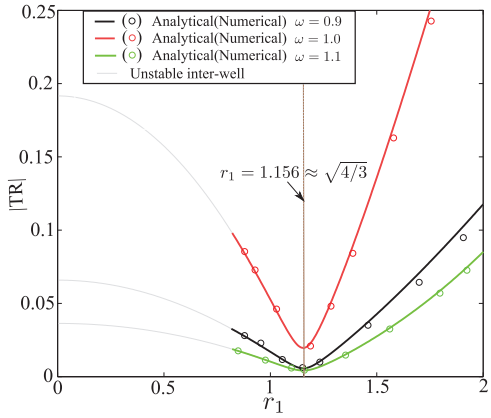

Figure 3. Force transmissibility of the valley response as a function of the bistable stage stroke amplitude.

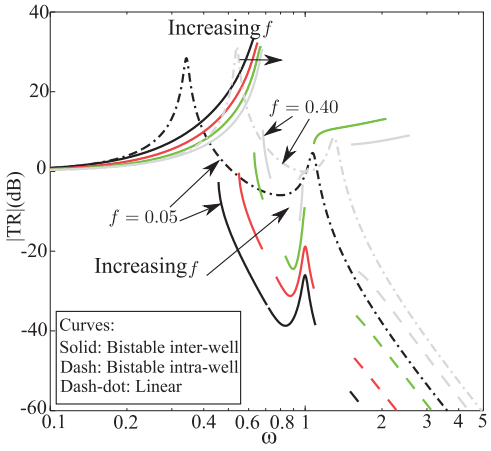

Figure 4. Force transmissibility comparison of the bistable and linear dual-stage isolators corresponding to the variation in frequency tuning ratio where $f = [0.05, 0.10, 0.20, 0.40]$.

model, to be dependent on initial conditions. The influence of initial conditions is carefully investigated and discussed in section 5.

3.2. Explanation of the valley response

The valley response exists within the frequency bandwidth corresponding to EIS and is a unique phenomenon due to bistability. Because the NLS nonlinear mechanism, which constitutes the bistable stage spring, contains two components to its overall restoring potential force—negative linear and positive cubic potential forces—the dynamic force supplied by one component may be counterbalanced by the other. Therefore, the linear stage of the isolator, which is subjected to the dynamic force of the bistable stage, will also possess a valley response and consequently will transmit a minimum of vibration to the foundation. A quantitative explanation of the phenomenon is provided by rewriting equation (5) as

$$y'' + \gamma_2 y' + y = \mu f F_{\text{bistable}} \tag{24}$$

$$F_{\text{bistable}} = \gamma_1 x' + f(-x + x^3). \tag{25}$$

Thus the vibration of the linear stage depends on the dynamic force F_{bistable}, which is determined by the stroke motion of the bistable stage. By substituting the inter-well solution into equation (25) and neglecting higher order terms, the fundamental amplitude of the dynamic force is determined to be $|F_{\text{bistable}}| = r_1\sqrt{(\omega\gamma_1)^2 + f^2[(3/4)r_1^2 - 1]^2}$. If $r_1 \to \sqrt{4/3}$ and $\gamma_1 \to 0$, the dynamic force will approach zero, and thus the excitation transmitted to the linear stage, and hence the foundation, will correspondingly approach zero. This is the valley response characteristic. Based on this interpretation, for a lightly damped bistable stage, the valley point (minimum of the valley response) will be obtained for any combination of excitation force p_0 and frequency ω so long as the bistable stage stroke amplitude $r_1 = \sqrt{4/3}$. To verify this conclusion, figure 3 shows force transmissibility of the valley response as a function of bistable stage stroke amplitude r_1 at three excitation frequencies, $\omega = 0.9$, 1.0, and 1.1. The loss factor $\gamma_1 = 0.01$ is selected for the bistable stage for the computations. Across each curve, excitation forces p_0 are varied to implement different stroke amplitudes r_1, whereas the excitation frequency ω is fixed. Therefore, for each curve in figure 3, r_1 in the horizontal axis is varied only with respect to the excitation force p_0 according to equation (14). In this figure, numerical results denoted by circles are presented for verification. Figure 3 shows that the valley point locations at the three frequencies are identical, and the corresponding stroke amplitudes are $1.156 \approx \sqrt{4/3}$. Numerical results are in good agreement with the analytical predictions. This verifies that the first-order harmonic balance method is accurate to obtain the steady-state responses of the bistable dual-stage isolator. The results also validate the consistent occurrence of the valley point minimum when the amplitude of the bistable stage stroke tends to $r_1 = \sqrt{4/3}$ due to specific combinations of excitation force p_0 and frequency ω, which serves as a useful design guideline for vibration isolation improvement.

4. Parametric study

To develop insights into effective bistable dual-stage isolator design, three parameters are selected for parametric study: the frequency tuning ratio of the first stage to the second stage f, the mass ratio of the first stage mass to the second stage mass μ, and the loss factor of the first stage γ_1. The initial parameters for simulations are $\mu = 1.0$, $f = 0.1$, $\gamma_1 = 0.05$, $\gamma_2 = 0.05$, and $p_0 = 1.0$. In the following studies, when one parameter changes, other parameters are retained at their initial values. Since each bistable dual-stage isolator's response in a figure contains three line types representing stable inter-well, stable intra-well and unstable solutions, for clear observation the unstable solution lines are omitted in the following.

4.1. Frequency tuning ratio

Figure 4 shows the responses corresponding to variation in frequency tuning ratio $f = [0.05, 0.10, 0.20, 0.40]$. The corresponding linear dual-stage isolator responses with frequency tuning ratios calculated by equation (23) are shown for cases of frequency tuning ratios of the bistable dual-stage isolator $f = 0.05$ and $f = 0.40$. As f increases, the isolation performance

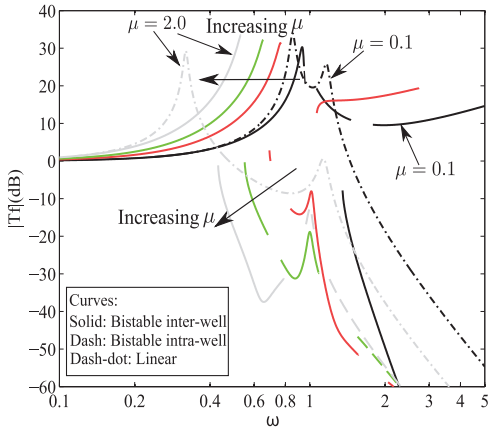

Figure 5. Force transmissibility comparison of the bistable and linear dual-stage isolators corresponding to variation in mass ratio where $\mu = [0.1, 0.5, 1.0, 2.0]$.

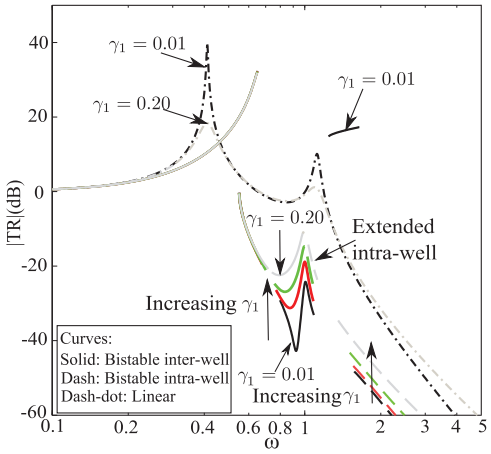

Figure 6. Force transmissibility comparison of the bistable and linear dual-stage isolators corresponding to a variation in loss factor of the first stage where $\gamma_1 = [0.01, 0.05, 0.10, 0.20]$.

of both bistable and linear systems degrades. Unlike the linear counterpart, the location of the second peak of the bistable dual-stage isolator is unaffected by the change of tuning ratio. For some higher values of tuning ratio $f \geq 0.20$, another branch of inter-well response may emerge and potentially coexist across portions of the intra-well frequency band. For higher f, the bandwidth of stable responses within the valley response diminishes. This indicates that it becomes more difficult to retain fundamental vibration in the valley response bandwidth so that beneficial isolation performance cannot be ensured. Therefore, for better isolation performance, the frequency tuning ratio needs to be small.

4.2. Mass ratio

The influence of the mass ratio μ is shown in figure 5, where $\mu = [0.1, 0.5, 1.0, 2.0]$. The first peak of the bistable dual-stage isolator shifts to a lower frequency as μ increases, which is the same trend exhibited by the linear counterpart's first peak. By increasing the mass ratio for the bistable dual-stage isolator, the beneficial valley response is stabilized, and the valley point frequency location moves to a lower frequency. It can also be seen that a large mass ratio may destabilize another inter-well response which overlaps the beneficial response for vibration isolation in the high frequency band where $\omega > 1.0$. Therefore, a large mass ratio improves the reliability of the bistable dual-stage isolator.

4.3. Loss factor of the first stage

Figure 6 demonstrates how changing the first stage loss factor γ_1 influences the response, where $\gamma_1 = [0.01, 0.05, 0.10, 0.20]$. When γ_1 increases, both resonant peaks of the linear dual-stage isolator are attenuated and the isolation performance at high frequencies degrades. Although the bistable dual-stage isolator has the same trend as the linear counterpart in the intra-well frequency band, the variation in the frequency band of the inter-well response is far different. The HEB responses are insensitive to a changing loss factor because the response bandwidths and amplitudes are nearly coincident, whereas the valley responses may become greater corresponding to an increase in γ_1. Around frequencies slightly higher than the second response peak for the bistable dual-stage isolator, an increasing loss factor γ_1 extends the existence of the intra-well response region towards the second peak, which suggests that it is more difficult to maintain inter-well response. The response of the valley point is lowest for smaller values of γ_1, which agrees with the interpretation in section 3.2 regarding a significant valley point attenuation magnitude if $\gamma_1 \to 0$. However, too small a bistable stage loss factor γ_1 (e.g. $\gamma_1 = 0.01$) may activate a high-energy branch of inter-well response for frequencies $\omega > 1.0$. The stable solution bandwidth in the valley response is also narrower for a decreased loss factor. Practically speaking, due to the strong nonlinearity, a very small loss factor γ_1 might lead to chaotic or quasi-periodic vibrations which are not conducive to isolation performance. Due to these observations, the influence of loss factor upon the likelihood of steady-state response will be further studied in the following section.

5. Influence of initial conditions

Initial conditions may affect solution outcomes for the bistable dual-stage isolator, which is a common factor for nonlinear systems [25]. Therefore, in this section, a large number of random initial conditions are chosen for simulations, to uncover the most repeatable nonlinear behaviors and determine the likelihood of beneficial responses for vibration isolation. The parameters for numerical integration are identical to those in figure 2. Taking $\omega = 0.8$ which is in the frequency band of the valley response as an example, the numerical responses of the bistable first stage are computed when the bistable dual-stage isolator has the initial conditions $(x_0, x_0', y_0, y_0') = (-1, 0, 0, 0)$ in figures 7(a)–(c) and $(x_0, x_0', y_0, y_0') = (0, 0, 0, 0)$ in figures 7(d)–(f).

Figure 7 presents, from left to right: the time series plot of the transmitted force p_t where $T = 2\pi/\omega$ in the horizontal axis represents the excitation period; the phase plot of bistable stage motion x and velocity x'; and the FFT of the

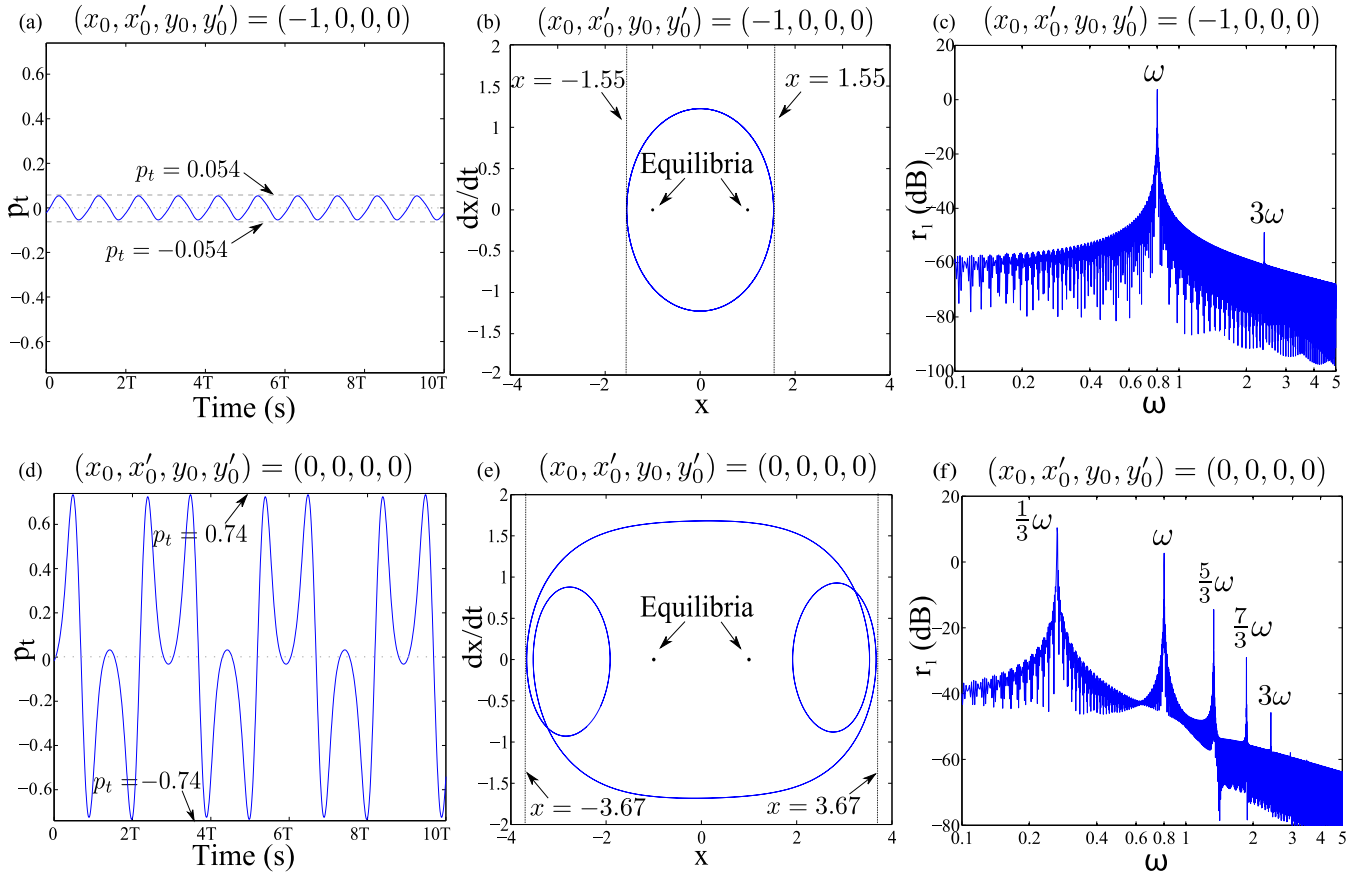

Figure 7. Numerical responses of the bistable dual-stage isolator at $\omega = 0.8$ subjected to two different initial conditions (x_0, x_0', y_0, y_0'): the top row $(-1, 0, 0, 0)$; the bottom row $(0, 0, 0, 0)$. From left to right: (a) and (d), time series plots of the transmitted force p_t; (b) and (e), phase plots of the bistable stage motion x and the velocity x'; (c) and (f), FFT plots of the bistable stage motion x.

response x. When initial conditions are $(-1, 0, 0, 0)$, figure 7 top row, the oscillation is single periodic valley response. When initial conditions are changed to $(0, 0, 0, 0)$, figure 7 bottom row, order-3 harmonic behaviors emerge, at frequencies $n\omega/3$ where $n = 1, 3, 5, \ldots$, and become a dominant contribution to the spectrum. As shown in the horizontal axes of figures 7(b) and (e), the overall amplitude of the bistable stage response x for initial conditions $(0, 0, 0, 0)$ is nearly twice that for $(-1, 0, 0, 0)$, which leads to a larger dynamic force imposed on the linear stage so that the isolation performance is significantly degraded, i.e. the maximum amplitude of the transmitted force $|p_t| = 0.054$ in figure 7(a) while $|p_t| = 0.74$ in figure 7(d). Figure 7 clearly demonstrates the large variation in response amplitude induced by either the single periodic valley response (top row) or the multi-harmonic behaviors (bottom row). This suggests that initial conditions should be closely investigated for design guidelines by which favorable isolation performance is ensured from the desired single periodic valley response.

To know the initial condition range which leads to the single periodic valley response and the best vibration isolation, a basin of attraction map at $\omega = 0.8$ is constructed using a 300 by 300 grid of (x_0, y_0) initial conditions. The map is determined by simulations where initial displacements of the stages are varied but all initial velocities are zero. This represents the isolator having various static loads and being excited from an initially stationary state. Figure 8 plots the basin map, where the black-shaded areas represent the initial conditions that lead to the single periodic valley response beneficial for vibration isolation, and white-shaded areas indicate the responses trending to multi-harmonic behaviors. Two unbroken regions of initial conditions stand out, representing a large range of configurations for which small deviations within these regions lead to the same final steady-state response. Since the relative areas of these two regions leading to either single periodic valley or multi-harmonic response are similar, the task of the designer is to ensure that the initial state of the isolator remains in the region leading to the beneficial single periodic valley response (the black-shaded region). It is seen that many such initial conditions in the unbroken black-shaded region have negative values, indicating that the bistable stage mass is closer to the linear stage mass from the start of excitation as seen in the schematic of figure 1; this finding may be advantageous in application because it indicates that the bistable dual-stage isolator is more 'compact' in the initial state that leads to the favorable single periodic valley response.

As mentioned in section 3.1, numerical results in figure 2 uncovered potential multi-harmonic responses in the frequency bandwidths $0.6 \leq \omega \leq 1.0$ and $1.1 \leq \omega \leq 1.6$. These multi-harmonic responses are dependent on initial conditions

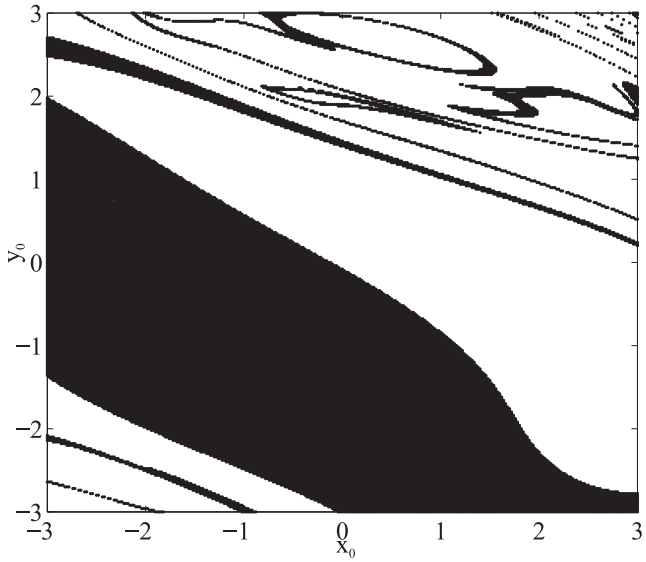

Figure 8. Basin of attraction map at $\omega = 0.8$. The initial condition ranges of x and y are from -3 to 3, respectively. Single periodic valley response, black-shaded area. Multi-harmonic response with $1/3\omega t$ component, white-shaded area.

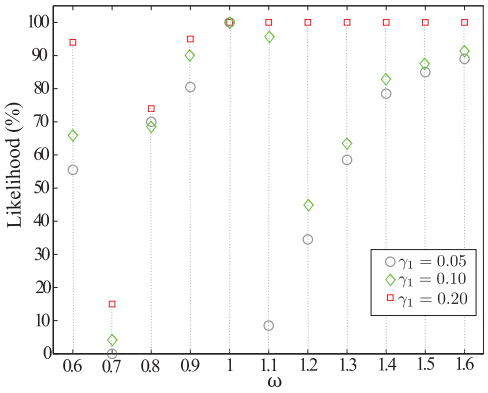

Figure 9. Percentage likelihood of the single periodic valley responses in $0.6 \leq \omega \leq 1.0$ and single periodic intra-well responses in $1.1 \leq \omega \leq 1.6$ for three cases of the bistable stage loss factor γ_1.

and may degrade isolation performance. For effective vibration isolation, the bistable dual-stage isolator must avoid these multi-harmonic responses and exhibit both the beneficial single periodic valley and the intra-well responses in $0.6 \leq \omega \leq 1.0$ and in $1.1 \leq \omega \leq 1.6$, respectively. Therefore, it is insightful to study the likelihood of the single periodic responses in this frequency band where multi-harmonic responses may occur. The initial conditions are $(x_0, x_0', y_0, y_0') = (-1 + \tilde{R}, 0, \tilde{R}, 0)$, where $\tilde{R}$ is a random variable satisfying a normal distribution with zero mean and unit standard deviation. The above initial conditions indicate that at the beginning of vibration control the system is stationary, whereas the displacement of either stage is randomly distributed around its negative equilibrium position, representative of various static loads upon the system.

Figure 9 presents the percentage likelihood that the isolator exhibits single periodic valley and intra-well responses for several cases of the bistable stage loss factor γ_1. These two forms of single periodic response—valley behaviors and intra-well oscillations—represent the favorable dynamics for isolation performance as demonstrated above, e.g., in figure 2(a). In figure 9, the discrete excitation frequencies from $\omega = 0.6$ to $\omega = 1.6$ are chosen, and 200 long-time responses under the random initial conditions are simulated at each frequency. The results in $0.6 \leq \omega \leq 1.0$ represent the percentage likelihood of single periodic *valley* responses, whereas the data in $1.1 \leq \omega \leq 1.6$ represent the percentage likelihood of single periodic *intra-well* responses. The alternative response form in both of these bandwidths (i.e. the remaining percentage), represents adverse multi-harmonic response outcomes. When $\gamma_1 = 0.05$, it is difficult to realize the single periodic valley response at $\omega = 0.7$ and single periodic intra-well response at $\omega = 1.1$. Overall, the likelihood of obtaining single periodic valley and intra-well response is increased for greater γ_1, and is exceptionally likely to occur for loss factor $\gamma_1 = 0.20$, which represents a loss factor that could be easily realized in practice. These findings indicate that larger damping of the bistable stage is beneficial to stabilize the single periodic dynamics and avoid multi-harmonic response so that effective isolation performance may be ensured.

6. Prototype investigations

A prototype of the bistable dual-stage isolator configured by cantilevered beams and mutually repulsive magnets is developed to verify the prior analytical predictions by numerical simulation and experiment.

6.1. Numerical quantitative verification

The prototype of the bistable dual-stage isolator is shown in figure 10(a). The bistable stage consists of two identical magnets and a cantilevered beam providing effective stiffness k_0. Damping tape is applied to the beam for the bistable stage damping d_1. The frame containing the bistable stage is connected to a second cantilevered beam which represents the linear stage stiffness k_2. Therefore, the frame and a portion of the second cantilevered beam represent the mass of the linear stage, and the displacement of the frame and the second cantilever beam tip represent the stroke motion of the linear stage. X_τ and Y_τ are the stroke motions of the bistable and linear stages, respectively. One magnet is fixed at the tip of the bistable stage's beam, whereas the other is fixed on the frame, and they are oriented so as to repulse each other. By decreasing distance Δ between magnets, the repulsive magnetic force buckles the beam, leading to two stable equilibria symmetric about the unstable equilibrium $X_\tau = 0$. The potential force of the bistable stage is [26]

$$F = k_0 X_\tau - 3HX_\tau (X_\tau^2 + \Delta^2)^{-\frac{5}{2}} \tag{26}$$

$$H = \frac{\eta_0 M^2}{2\pi} \tag{27}$$

where η_0 and M are free permeability and magnetic pole strength, respectively. The potential force F may be expanded

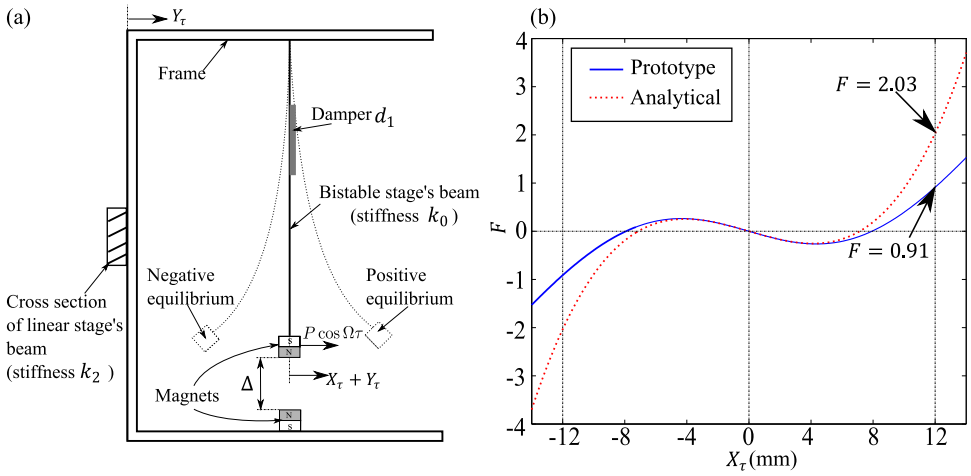

Figure 10. (a) Schematic of a prototype of the bistable dual-stage isolator configured by cantilevered beams and mutually repulsive magnets, and (b) the bistable stage's potential forces F of the prototype and analytical model with respect to the bistable stage's stroke X_τ.

by Taylor series to

$$F = -k_1 X_\tau + k_3 X_\tau^3 - \frac{105H}{8\Delta^9} X_\tau^5 + \cdots \tag{28}$$

where

$$k_1 = \left(\frac{3H}{\Delta^5} - k_0\right); \tag{29}$$

$$k_3 = \frac{15H}{2\Delta^7}; \tag{30}$$

and

$$\Delta < \left(\frac{3H}{k_0}\right)^{1/5}.$$

There exists a deviation between the restoring force employed in the analytical model of section 2 and the exact force expression of the specific prototype design considered in this section, which is given by equation (26). The deviation is reflected by the higher order terms in the Taylor series expansion which are neglected by the analytical model, $-(105H/8\Delta^9)X_\tau^5 + \cdots$. Thus, as regards the prototype configuration, the analytical model employs a potential force expression of $F = -k_1 X_\tau + k_3 X_\tau^3$ where k_1 and k_3 are given by equations (29) and (30). Figure 10(b) compares the two force expressions, equation (26) and the prior analytical model expression, to demonstrate the deviation. The parameters are $\eta_0 = 4\pi \times 10^{-7}$ N A^{-2} and $M = 1.74$ A m^2 while the distance between magnets is $\Delta = 0.022$ m. The stiffness of the bistable stage cantilevered beam is $k_0 = 260$ N m^{-1}; therefore, by the analytical model expression, the stable equilibria of the bistable stage are approximately located at $X_\tau = \pm\sqrt{k_1/k_3} = \pm 7$ mm. Figure 10(b) shows that the deviation of the bistable stage potential forces between the prototype and the analytical model becomes non-trivial if the stroke X_τ is considerably larger than the stable equilibria value. The result indicates that analytical model predictions of the prototype response, as studied in this section, will be accurate so long as the bistable stage exhibits EIS or intra-well dynamics, in which case stroke motion remains small.

To evaluate the validity of earlier analytical findings that employed the reduced-order potential force expression

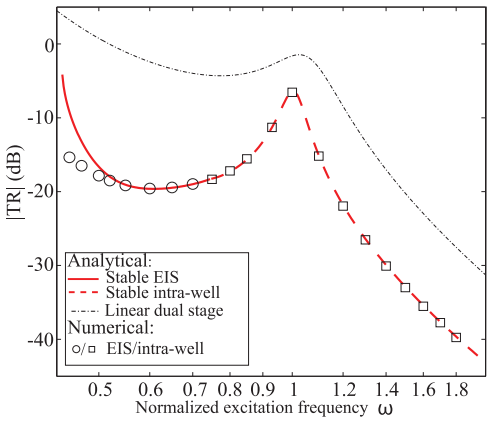

Figure 11. Force transmissibility of the force P_t to the excitation force P as a function of normalized excitation frequency ω.

against the exact expression in equation (26) for the prototype studied in this section, numerical simulations of the governing equations of the bistable dual-stage isolator are conducted using the full potential force expression in equation (26) for the bistable stage. In the simulation, the bistable stage mass is $m_1 = 0.23$ kg. The linear stage mass is $m_2 = 0.23$ kg and stiffness is $k_2 = 9270$ N m^{-1}. As found in figure 9, a large bistable stage loss factor γ_1 is conducive to stabilization of the single periodic dynamics; thus, to ensure the single periodic EIS and intra-well responses are obtained, γ_1 is chosen to be 0.4 in the simulation. Finally, damping of the linear stage is $\gamma_2 = 0.05$ while the excitation amplitude is $P = 30$ N.

Figure 11 presents the force transmissibility of the transmitted force P_t to the excitation force P. The numerical simulation results of the prototype are in very good agreement with the analytical predictions across the bandwidth. Due to the stabilization effect of the large loss factor γ_1, the simulations predict that the bistable dual-stage isolator exhibits only the single periodic EIS or intra-well responses. Figure 11 indicates that the bistable dual-stage isolator significantly outperforms the linear counterpart in the frequency band. The good agreement between numerical and analytical results validates the

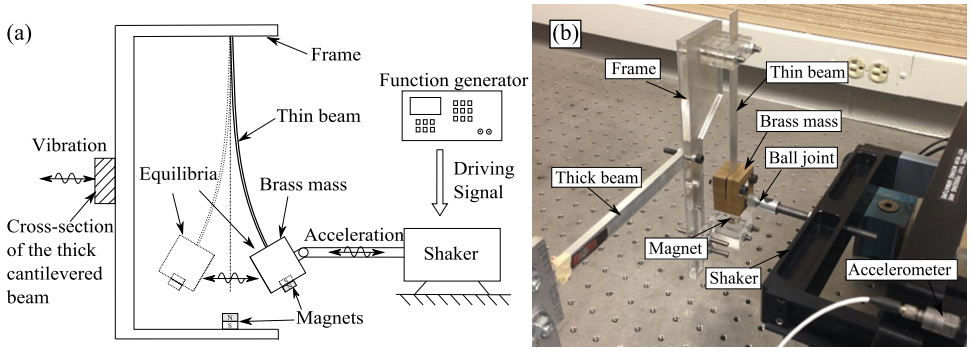

Figure 12. Experimental setup: (a) schematic and (b) photograph, to validate the valley response of a bistable dual-stage isolator prototype.

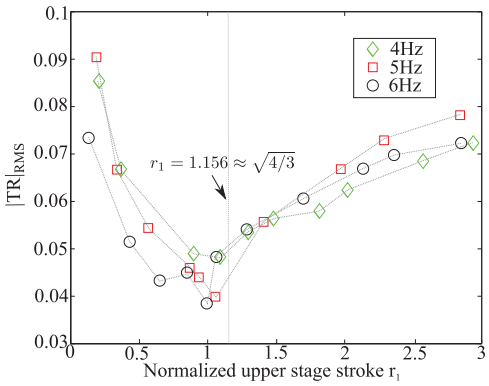

Figure 13. RMS transmissibility as a function of normalized bistable stage stroke.

conclusions drawn from the earlier analytical investigations using the fundamental harmonic balance approach and simplified potential force expression, and moreover demonstrates the viability of the bistable dual-stage isolator employing the configuration of the present prototype.

6.2. Experimental qualitative validation

An experimental setup is constructed to demonstrate the valley response attenuation capability of the bistable dual-stage isolator prototype shown in figure 10(a). A schematic and a photograph of the setup are provided in figures 12(a) and (b), respectively. The bistable stage consists of a cantilevered thin aluminum beam (length: 99.0 mm; width: 13.0 mm; thickness: 1.3 mm), two repulsive magnets and a brass mass (0.225 kg). One of the magnets is embedded in the brass mass fastened at the tip of the beam, whereas the other is fixed to a frame, and they are oriented so as to repulse each other. The bistable stage's stable equilibria are ± 5 mm from the center line.

In this experiment, the brass mass of the bistable stage is connected to the shaker armature with a ball joint to minimize torsional influences during shaker excitation. The frame and a portion of the thick cantilevered beam represent the mass of the linear stage, and the tip displacement represents the stroke motion of this stage. The shaker excitation constitutes displacement- or acceleration-controlled input as compared to constant periodic force. Therefore, the bistable stage mass connected to the shaker armature is driven to exhibit single periodic vibration. By varying the control signal of the shaker, the bistable stage will exhibit harmonic vibrations of varied stroke amplitudes. This allows direct verification of the valley phenomenon as earlier studied through figure 3. By equation (18), the transmitted vibration force is proportional to the vibration amplitude of the linear stage at a specified frequency. Thus, vibration isolation can be expressed by dividing the root mean square (RMS) of the linear stage's steady-state stroke by the RMS of the shaker's steady-state stroke. Therefore, the RMS transmissibility is

$$|\mathrm{TR}|_{\mathrm{RMS}} = \frac{\sqrt{\frac{1}{T}\int_0^T |Y_\tau|^2 \,\mathrm{d}\tau}}{\sqrt{\frac{1}{T}\int_0^T |A_\tau|^2 \,\mathrm{d}\tau}} \tag{31}$$

where Y_τ and A_τ are the steady-state strokes of the linear stage and the shaker, and T is the sampled time used for integration.

The parameters of the bistable stage are obtained by system identification. Then, the length of the thick beam is adjusted so that the frequency tuning ratio $f \approx 0.1$, which was also used in figure 3 to interpret the valley response. The ratio of bistable first stage mass to linear second stage mass is $\mu \approx 1.0$. The loss factors of the bistable stage and the linear stage are $\gamma_1 \approx 0.025$ and $\gamma_2 \approx 0.05$, respectively. A function generator and an amplifier drive the shaker at frequencies of 4, 5, and 6 Hz, where the shaker is able to produce sufficient sinusoidal stroke. An accelerometer (PCB 352C04) and a laser vibrometer (Polytec OFV-3001) measure the shaker acceleration and the vibration displacement of the thick beam's tip (i.e. response of the linear stage), respectively.

Figure 13 presents the force transmissibility as a function of bistable stage stroke normalized by the value of the stable equilibrium. The experimental results show the minimum of the valley response is consistently obtained so long as the key bistable stage stroke amplitude r_1 is achieved, verifying the analytical observations in section 3.2. The normalized bistable stage stroke corresponding to the minima at each frequency is found to be between 1.0 and 1.1, which is also in good agreement with the analytically predicted value $\sqrt{4/3} \approx 1.156$. There is deviation between the trends of the slopes of the curves predicted analytically and measured experimentally; this is attributed to the experimental configuration for which the repulsive magnetic dipole and bistable stage beam do not

exactly realize negative linear and positive cubic potential forces, and to the use of the ball joint containing a small damping material that dissipates higher frequency vibration. Apart from this minor discrepancy in trends, the experimental results are in very good agreement with the analyses regarding attainment of the valley response and its specific minimum as defined by the bistable stage stroke.

7. Conclusion

This paper investigated steady-state performance of a bistable dual-stage vibration isolator, which brings together the opportunities of force counterbalance unique to bistable systems and the improved isolation performance abilities of dual-stage designs. Response phenomena beneficial for isolation enhancement are analytically predicted and validated through numerical studies. Based on analyses of the fundamental periodic vibration, it is found that the bistable dual-stage isolator may outperform an equivalent linear dual-stage isolator over a significant frequency bandwidth. It is shown that a valley response, the unique phenomenon of the bistable dual-stage isolator due to counterbalance of its potential forces, improves isolation performance and that attainment of the valley response minimum is ensured by realizing a key amplitude of bistable stage displacement stroke. The basin of attraction mapping illustrates initial condition dependence leading to either the beneficial single periodic valley behavior or the multi-harmonic response in a portion of the frequency bandwidth that leads to excitation induced stability. It is shown that increasing the bistable stage damping is conducive to stabilization of the single periodic responses for effective vibration isolation. Finally, numerical and experimental investigations of a prototype quantitatively and qualitatively validate the analytical predictions and demonstrate the robust performance of the bistable dual-stage isolator design.

Acknowledgments

This work is partially supported by China Scholarship Council funding (No. 201206020092) and the University of Michigan Collegiate Professorship fund.

References

[1] Rivin E I 1995 Vibration isolation of precision equipment *Precis. Eng.* **17** 41–56
[2] DeBra D B 1992 Vibration isolation of precision machine tools and instruments *CIRP Ann. Manuf. Technol.* **41** 711–8
[3] Carrella A, Brennan M J and Waters T P 2007 Static analysis of a passive vibration isolator with quasi-zero-stiffness characteristic *J. Sound Vib.* **301** 678–89
[4] Ibrahim R A 2008 Recent advances in nonlinear passive vibration isolators *J. Sound Vib.* **314** 371–452
[5] Platus D L 1992 Negative-stiffness-mechanism vibration isolation systems *Proc. SPIE* **1619** 44–54
[6] Yang J, Xiong Y P and Xing J T 2013 Dynamics and power flow behaviour of a nonlinear vibration isolation system with a negative stiffness mechanism *J. Sound Vib.* **332** 167–83
[7] Ahn H-J 2008 Performance limit of a passive vertical isolator using a negative stiffness mechanism *J. Mech. Sci. Technol.* **22** 2357–64
[8] Carrella A, Brennan M J, Kovacic I and Waters T P 2009 On the force transmissibility of a vibration isolator with quasi-zero-stiffness *J. Sound Vib.* **322** 707–17
[9] Carrella A, Brennan M J, Waters T P and Lopes V Jr 2012 Force and displacement transmissibility of a nonlinear isolator with high-static-low-dynamic-stiffness *Int. J. Mech. Sci.* **55** 22–9
[10] Lu Z, Brennan M J, Yang T, Li X and Liu Z 2013 An investigation of a two-stage nonlinear vibration isolation system *J. Sound Vib.* **332** 1456–64
[11] Ibrahim R A 2006 Excitation-induced stability and phase transition: a review *J. Vib. Control* **12** 1093–170
[12] Kim S-Y and Kim Y 2000 Dynamic stabilization in the double-well Duffing oscillator *Phys. Rev.* E **61** 6517–20
[13] Kim Y, Lee S Y and Kim S-Y 2000 Experimental observation of dynamic stabilization in a double-well Duffing oscillator *Phys. Lett.* A **275** 254–9
[14] Wu Z, Harne R L and Wang K W 2014 Excitation-induced stability in a bistable Duffing oscillator: analysis and experiments *ASME J. Comput. Nonlinear Dyn.* at press
[15] Harne R L and Wang K W 2013 A review of the recent research on vibration energy harvesting via bistable systems *Smart Mater. Struct.* **22** 023001
[16] Pellegrini S P, Tolou N, Schenk M and Herder J L 2013 Bistable vibration energy harvesters: a review *J. Intell. Mater. Syst. Struct.* **24** 1303–12
[17] Johnson D R, Thota M, Semperlotti F and Wang K W 2013 On achieving high and adaptable damping via a bistable oscillator *Smart Mater. Struct.* **22** 115027
[18] Johnson D R, Harne R L and Wang K W 2014 A disturbance cancellation perspective on vibration control using a bistable snap through attachment *J. Vib. Acoust.* doi:10.1115/1.4026673
[19] Dong L and Lakes R S 2012 Advanced damper with negative structural stiffness elements *Smart Mater. Struct.* **21** 075026
[20] Harne R L and Wang K W 2013 Robust sensing methodology for detecting change with bistable circuitry dynamics tailoring *Appl. Phys. Lett.* **102** 203506
[21] Younis M I, Ouakad H M, Alsaleem F M, Miles R and Cui W 2010 Nonlinear dynamics of MEMS arches under harmonic electrostatic actuation *J. Microelectromech. Syst.* **19** 647–56
[22] Tseng W-Y and Dugundji J 1971 Nonlinear vibrations of a buckled beam under harmonic excitation *J. Appl. Mech.* **38** 467–76
[23] Blair K B, Krousgrill C M and Farris T N 1997 Harmonic balance and continuation techniques in the dynamic analysis of Duffing's equation *J. Sound Vib.* **202** 717–31
[24] Szemplińska-Stupnicka W and Rudowski J 1993 Steady-states in the twinwell potential oscillator: computer simulations and approximate analytical studies *Chaos* **3** 375–85
[25] Virgin L N 2000 *Introduction to Experimental Nonlinear Dynamics: A Case Study in Mechanical Vibration* (Cambridge: Cambridge University Press)
[26] Tang L, Yang Y and Soh C-K 2012 Improving functionality of vibration energy harvesters using magnets *J. Intell. Mater. Syst. Struct.* **23** 1433–49